Materials Horizons

Alloying multiple halide perovskites on the same sublattice in search of stability and target band gaps

Journal:	*Materials Horizons*
Manuscript ID	MH-COM-03-2025-000540.R1
Article Type:	Communication
Date Submitted by the Author:	03-Jun-2025
Complete List of Authors:	Sabino, Fernando; Universidade de São Paulo Escola de Engenharia de São Carlos, Departamento de Engenharia de Materiais ; University of Colorado Boulder, Renewable and Sustainable Energy Institute; Universidade de São Paulo Instituto de Física, Departamento de Física dos Materiais e Mecânica Xiong, Jiaxin; University of Colorado Boulder, Renewable and Sustainable Energy Institute Zhang, Xiuwen; University of Colorado Boulder, Renewable and Sustainable Energy Institute Dalpian, Gustavo; Universidade de Sao Paulo Instituto de Fisica, Departamento de Física dos Materiais e Mecânica Zunger, Alex; University of Colorado Boulder, Renewable and Sustainable Energy Institute

New Concepts

This work presents a systematic alloy design strategy for halide perovskites (HPs) to achieve simultaneous band gap tuning and structural stability by exploring multiple compositional degrees of freedom. We consider (i) substitutions across different sublattices (A-, B-, and X-sites), (ii) mixing of both isovalent (Sn,Pb) and hetero-valent (Sn,Cd) species, and (iii) incorporation of multiple elements within each given sublattice. Using the polymorphous network model, whereby even a single substituent can lower the systems total energy by acquiring a distribution of different local environments, we capture local distortions while preserving global cubic symmetry, thus providing a more realistic representation of alloy behavior. Unlike previous studies limited to binary mixing or idealized non polymorphous networks, our approach investigates a broader compositional space and examines the interplay between disordered alloys and ordered double perovskites, offering key insights into phase stability. Our findings reveal that X-site (halogen) and A-site (alkaline) enabling precise band gap control, while B-site alloying has the most significant effect on band gap modulation, with Sn-Pb (isovalent) alloys exhibiting positive bowing and Cd-Pb (hetero-valent) alloys showing negative bowing. Additionally, we identify conditions where ordered phases emerge from disordered alloys, guiding the synthesis of stable, high-performance HP materials. These insights establish fundamental design principles for next-generation optoelectronic materials, balancing electronic tunability and structural stability.

Data availability statements

Data for this article, including the alloys chemical composition, band gap and total energy, all of them calculated with density functional theory, are available at Gitbub at https://github.com/fernandopsabino/data_alloys_HP.

Alloying multiple halide perovskites on the same sublattice in search of stability and target band gaps

Fernando P. Sabino[1,2,3], Jia-Xin Xiong[2], Xiuwen Zhang[2], Gustavo M. Dalpian[3], Alex Zunger[2]

1 Department of Materials Engineering, São Carlos School of Engineering, University of São Paulo, São Carlos, SP 13563-120, Brazil

2 Renewable and Sustainable Energy Institute, University of Colorado, Boulder, Colorado 80309, USA.

3 Institute of Physics, University of São Paulo, São Paulo, SP 05508-090, Brazil

Single-component halide perovskites (HPs) rarely satisfy all the necessary criteria for optoelectronic applications, such as achieving an optimal band gap while maintaining high chemical and structural stability. Alloying halide perovskites has emerged as a promising strategy, not only to enhance stability but also to fine-tune their electronic and optical properties. In this work, we explore multiple degrees of freedom in alloy design, considering different substitution sublattices sites (A, B, or X in ABX_3 perovskites), various chemical species (isovalent and hetero-valent elements), and multi-component compositions on a given sublattice. Using first-principles calculations based on density functional theory (DFT), we investigate how compositional variations influence the electronic (band gap) and structural properties (mixing enthalpy) of HP alloys. Our approach employs the polymorphous cell model, allowing full local relaxation which breaks local symmetry while preserving global cubic symmetry—an essential framework for accurately modeling HPs. Our results reveal that X-site mixing (halogen substitution) primarily affects the valence band maximum, allowing target band gap engineering. Additionally, variations in halogen radii introduce internal strain through octahedral distortions, influencing the mixing enthalpy. A-site substitution, while not directly contributing to the band edge states, modifies structural stability via volume effects, indirectly impacting the band gap. B-site alloying plays a dominant role in band gap modulation, leading to either positive or negative band gap bowing. Specifically, isovalent B-site mixing (Sn-Pb) induces strong positive bowing, where the alloy band gap is smaller than the average gap of parent compounds, whereas hetero-valent mixing (Cd-Pb) results in pronounced negative bowing. As an aside, we investigate the competition between the excess energy of disordered alloys vs. that of long-range ordered double perovskites of the same compositions, seeking examples of ordered phases emerging from disordered alloys. Our findings provide fundamental insights into the electronic and structural behavior of HP alloys, offering valuable design principles for the development of stable and efficient materials for next-generation photovoltaic and optoelectronic devices.

Keywords: Halide perovskites, Halide perovskites alloys, electronic structure, multi-component alloys.

1. Introduction

Single-component halide perovskites (HPs) with the general formula ABX_3 have emerged as promising materials for optoelectronic applications, including solar cells, LEDs, and radiation detectors[1–4]. However, a single compound HP rarely meets all the desired properties simultaneously, such as an optimal band gap and high chemical and structural stability[1–3,5,6]. A widely explored approach to overcome these limitations involves forming halide perovskite alloys by combining different elements at the A, B, or X sites[4,7–9]. Alloying provides additional degrees of freedom, including: (i) alloying elements in different sublattices: A(1+), X(1-) and B(2+); (ii) mixing either isovalent species from the same Periodic Table column (e.g., Pb and Sn at the B-site) or hetero-valent species from different Periodic Table Columns (e.g., Sn and Cd at the B-site); and (iii) incorporating multiple elements at a single lattice site ("multiple substitution").

The properties of HP alloys are highly dependent on the nature of the orbitals introduced by different substituents on the alkaline cation A sublattice, the metalloid B sublattice, and the halogen X sublattice. This tunability leads to changes in the band edge orbital character (BEOC), which affects the electronic and optical properties and indirectly influences structural stability. Figure 1 schematically illustrates the band composition across the A, B, and X sites, using standard perovskite compounds such as MAPbI3 and CsPbBr3 as examples.

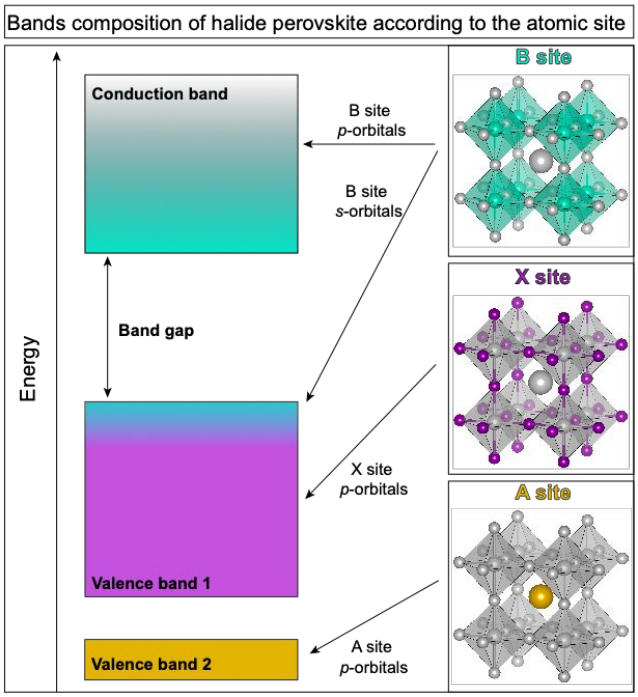

Fig. 1: Schematic representation of the electronic orbitals contributing of halide perovskites to different states, highlighting the orbital contributions from each atomic site. This system is exemplified using standard halide perovskites, such as $MAPbI_3$ or $CsPbBr_3$. The band composition is color-coded to match the corresponding atomic sites. The valence band 1 represents the highest occupied electronic state.

From previous results in the literature, and as shown in Fig. 1, halogen on X site affects the orbital energies near the valence band maximum (VBM), thus, halogen alloying can directly affect the band gap in the system. For instance, mixing Br and I in varying ratios in $MAPb(I_xBr_{1-x})_3$, enables allowing adjustment of the band gap from 1.56 eV to 2.23 eV[7]. This tunability creates opportunities for using halide perovskites in tandem solar cells, where specific band gaps are targeted. However, halide

perovskites with intermediate I and Br concentrations can undergo light-induced phase segregation, creating I- or Br-rich regions—a phenomenon known as the Hoke effect [8,10]. Adding the alloy degree of freedom by introducing ternary or multinary alloys may help mitigate this effect, improving the stability of halide perovskites under light exposure[11].

Fig. 1 also shows that the alkaline orbitals of the A sublattice do not contribute to the states near the band edges (VBM or conduction band minimum - CBM), so it was supposed not to have direct effects on the band gap. As alkali substitution does change the molar volume of the alloy (size effect), this can affect the band gap indirectly via internal pressure effect. Diversifying the A site composition helps alleviate this strain, thereby improving the structural stability of halide perovskites. Currently, one of the most efficient HP-based solar cells utilizes a mixed-cation composition of $(Cs_{0.05}FA_{0.85}MA_{0.1})PbI_3$, which combines different elements at the A site to achieve optimal performance[4].

The atoms on the B sublattice in halide perovskites can manipulate the orbitals composition of both valence and conduction bands and contribute to states near the band edges, as shown in Fig. 1, and, like halogen mixing, modifications at the B site directly affect the band gap values of halide perovskites. Theoretical studies suggest that mixing Pb and Sn can result in significant positive band gap bowing, i.e., for certain Pb-Sn concentrations, the alloy band gap is smaller than that of either parent compound—a behavior similar to that observed in $CdTe_xSe_{1-x}$ alloys[9,12–14]. In addition, in conventional semiconductors (GaAs), the cation s-orbital is unoccupied and, in general, composes the states of conduction band. For semiconductors with heavy cation atoms (e.g. Pb), the s-orbitals will exist in the occupied valence band, which is observed in lead chalcogenides[15]. The manipulation and alloy creation in these systems can directly affect the orbital composition, the absolute value of the band gap and the nature of the band gap (indirect vs. direct). This effect is also possible in halide perovskites.

The current work addresses the question of how the electronic properties change by considering different alloy compositions and concentrations in the context of first principles electronic structure theory, focusing on the parallel band gaps and stability. This is not a shot-gun high-throughput approach, focusing instead on specific examples of each of the degrees of freedom noted above. Our results suggest that elements in the X and A sites allow for fine-tuning of the band gap, with mixing enthalpy strong dependent of the octahedral tilting. In contrast, elements in the B site can induce significant changes in the band gap, either downward bowing or upward bowing it, depending on the specific cation used. The physical insights discussed here can be extended to other halide perovskite alloys, providing a foundation for future studies. It is also important to note that our approach does not account for the influence of point defects on the electronic structure of halide perovskites. Previous studies have shown that point defects can significantly impact the optoelectronic performance of materials by inducing charge localization and creating states within the band gap[16–18]. However, for single halide perovskite compounds, most intrinsic point defects are generally considered to form shallow states[19–21], with the notable exception of iodide interstitials, which have been reported to introduce deep levels[19,22].

II. Theoretical approach and computational details

The difficulty of getting a realistic description of halide perovskites within density functional theory (DFT) is handled as follows: (i) Polymorphous cell, i.e. different local environments are allowed even for the same chemical elements in the solid. This entails using a larger than minimal unit cell. Cases include the possibility to describe octahedral rotation, atom displacement and bond disproportionation. This structure is used when the total energy, E_{Tot}, reduced when compared to high symmetry system[8,9,19,23–25]. (ii) We focus in this study on cubic systems. To describe the HP systems, a supercell with cubic shape (fixed volume and fixed shape) is used, however internal atomic positions are allowed to relax. The relaxation is done by using the

Perdew-Burke-Ernzerhof exchange correlation functional as implemented for solids (PBESol)[26]. The lattice parameter for the alloy was determined by a linear interpolation according to the Vegard's law for different alloy concentration. (iii) Relativistic correction included via spin-orbit coupling (SOC). (iv) Electronic structure of the final relaxed system is calculated by hybrid exchange and correlation function, using Heyd-Scuseria-Ernzerhof (HSE)[27,28] with SOC, but empirically adjusting the exact exchange to 43% to reproduce the band gap of most studies single halide perovskites. Table I shows the results for single perovskites vs experiment data.

The alloys band gap energy $E_g^{Alloy}(x,y)$ and the alloy total energy $E_{Tot}^{Alloy}(x,y)$ with respect to the corresponding quantities as a linearly weighted interpolation of the constituent cubic single perovskites gap E_g^{α} and total energy E_{Tot}^{α} compose two important physical property that is fundamental for alloys interpretation: The band gap variation ΔE_g and the mixing enthalpy ΔH, that are calculated by the following equation, respectively:

$$\Delta E_g = E_g^{Alloy} - \left[xE_g^{\alpha} + yE_g^{\beta} + (1-x-y)E_g^{\gamma}\right], \quad [1]$$

$$\Delta H = E_{Tot}^{Alloy} - \left[xE_{Tot}^{\alpha} + yE_{Tot}^{\beta} + (1-x-y)E_{Tot}^{\gamma}\right]. \quad [2]$$

The quantities of the constituent single perovskites are calculated at their respective equilibrium lattice constants, while the alloy properties are determined at the alloy lattice constant. The alloy configuration is modeled in a special supercell where alloying atoms occupy lattice sites in a pattern that approximates a random distribution as closely as possible within a finite-size supercell, known as a special quasi-random structure (SQS)[29,30]. These computational choices are fundamental to obtaining a good approximation to realistic halide perovskite measured properties.

Technical details: Our density functional theory (DFT) calculation is done as implemented in the Vienna ab-initio simulation package (VASP)[31,32]. The interaction between valence electrons and the ionic cores is treated according to the projected augmented wave (PAW) method[33,34]. The cutoff energy of 450 eV is used for the plane wave expansion during the minimization of the stress tensor. At the same time, the forces are minimized on all atoms until they become smaller than 0.01 eV/Å. For the Brillouin zone integration in the cubic Pm-3m cell, we use a k-mesh of 7x7x7 for $CsPbI_3$ and the same k-density for all the remaining compositions.

The polymorphous cell is constructed based on a repetition of $2\sqrt{2}$x$2\sqrt{2}$x4 of volume optimized Pm-3m cubic perovskites, resulting in a supercell composed of 32 ABX_3 f.u. (160 atoms)[23]. In this polymorphous configuration, we nudge the atoms by a random displacement within 0.15 Å in all directions, and in the sequence, we relax the atomic forces (keeping the volume constant) using PBESol. Because of the large supercell of the polymorphous configuration, we use only the Γ-point for the Brillouin zone integration. The concentration of each chemical specie is allowed to vary in the range $0.0 < x < 1.0$, and in intervals of 0.125.

III. Results

In this study, we present the properties of halide perovskite alloys with different chemical compositions across different substitution sites. To organize our findings, we divide the results section into five main categories: (i) Alloying multi-Halogen ions on the X-sublattice, as exemplified by $CsPb(I_xBr_yCl_{1-x-y})_3$; (ii) Alloying multi-Alkali cations on the A-sublattice, as exemplified by

$(Cs_xRb_yK_{1-x-y})CsBr_3$; (iii) Alloying multi column-IV cations on the B-sublattice, as exemplified by $Cs(Pb_xSn_yGe_{1-x-y})Br_3$; (iv) Same as (iii) but using hetero-valent cations on the B-sublattice , as exemplified by $Cs(Pb_xSn_yCd_{1-x-y})Br_3$; and (v) comparison of alloys configuration and high ordered double perovskites.

Table I: Lattice parameters (a_0), band gap (E_g), and geometrical tolerance factor, Goldschmidt (t) and the new factor (τ) for the parent compounds used in creating the triple-mixed halide perovskite. Experimental data is included in the table when available.

System	a_0 (Theory) (Å)	a_0 (Exp.) (Å)	E_g (theory) (eV)	E_g (Exp.) (eV)	Goldschmidt (t)	New factor τ
$CsPbI_3$	6.26	6.29[35]	1.67	1.73 [36]	0.85	4.30
$CsPbBr_3$	5.86	5.85[37]	2.17	2.23 [38]	0.86	4.10
$CsPbCl_3$	5.61	5.60[39]	2.71	3.00[40]	0.87	3.98
$RbPbBr_3$	5.85		2.45		0.83	4.57
$KPbBr_3$	5.84		2.66		0.81	4.94
$CsSnBr_3$	5.76	5.79[41]	1.53	1.80[42]	1.02	3.37
$CsGeBr_3$	5.48		1.37		1.01	3.37
$CsCdBr_3$	5.48		2.99		0.93	2.11

Before introducing the alloys, it is important to describe the properties of single halide perovskites, that are building blocks to constructure the alloy configuration. Table I provides the band gaps, lattice parameters, Goldschmidt tolerance factor t[43], and the new tolerance factor τ[44] for each parent compounds that are used as building blocks to compose the alloy, along with corresponding experimental results when available. These lattice parameters are used to calculate the volume and, following Vegard's law, to determine the volumes of each alloy. Notably, all parent compounds and alloys are modeled in a cubic perovskite polymorphic supercell, having the global symmetry of the cubic Pm-3m structure but non-cubic local site symmetries. Among the perovskite phases, the cubic configuration, compared to tetragonal or orthorhombic forms, generally remains the most stable configuration at temperatures near room temperature.

A. Alloying multi-Halogen ions on the X sublattice: $CsPb(I_xBr_yCl_{1-x-y})_3$

Absolute magnitude of the band gaps of halide perovskite X-site random alloys. In Fig. 2(a), we show the compositional triangle for $CsPbI_3$-$CsPbBr_3$-$CsPbCl_3$ with band gap values calculated on the discrete compositional grid. In halide perovskites, the halogen atoms contribute to the states near the VBM, as illustrated in Fig. 1, and modifications in the chemical composition on this site directly impact the band gap. First, looking at the parent compounds, we observe a correlation between the band gap and the atomic radius of the halogen, smaller halogens like Cl lead to larger band gaps, while larger halogens like I result in smaller band gaps, as shown in Table I and observed in the corners of the triangle in Fig. 2(a). This correlation is reflected in the halogen mixing alloys, where incorporating small (large) halogen atoms leads to band gap opening (narrowing). It is also important to note in Fig. 2(a) that, the band gap variation across the alloy chemical composition does not change abruptly, creating valleys or peaks in the phase diagram, indicating that halogen mixing is a good parameter to fine-tune the band gap of halide perovskites. The second important characteristic of halogen mixing alloys is that the band gap is always confined by the band gaps of the parent compounds, i.e., no halogen alloy composition can produce a band gap larger than $CsPbCl_3$ (2.71 eV) or smaller than $CsPbI_3$ (1.67 eV).

Deviation of the band gaps of halide perovskite X-site random alloys from the composition weighted averages. The deviation of the band gap with respect to the parent alloys is calculated according to Eq. [1], where E_g^{α} is the band gap of alloy

component α represented here by $CsPbI_3$; E_g^{β} is the band gap of alloy parent β that is represented here by $CsPbBr_3$; and E_g^{γ} is the band gap of alloy parent γ that is represented here by $CsPbCl_3$. All the parent compounds are taken at its own free-space unit cell equilibrium volume (lattice constant shown in Table I). The index x and y are the alloy concentration of $CsPb(I_xBr_yCl_{1-x-y})_3$. The results for band gap variation for halogen mixing alloys are shown in Fig. 2(b).

We observe that the variation of the calculated alloys band gap with respect to the linear interpolation for halogen mixing site is minimal. All the results are between -60 to 60 meV which refer to the order of less than 5% of the linear interpolation for $CsPb(I_xBr_yCl_{1-x-y})_3$. This small variation indicates that we can estimate the alloy band gap in halogen mixing site by a simplest linear interpolation.

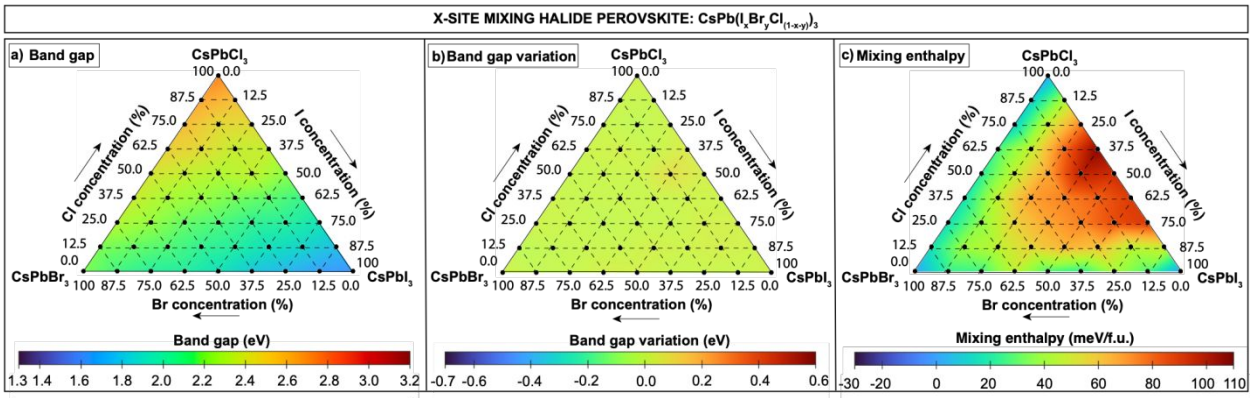

Figure 2: X-site halogen mixing alloys, using as example $CsPb(I_xBr_yCl_{1-x-y})_3$. (a) Absolute magnitude of Band gaps for halide perovskite alloys (b) Band gap variation considering Eq. 1. (c) Alloy mixing enthalpy calculated using Eq. 2.

Mixing enthalpies and structural stability of halide perovskite X-site random alloys. Beyond the band gap, considering the stability with respect to the parents' compounds of halide perovskite alloys is also important. According to structural stability criteria (geometry), based on the Goldschmidt tolerance factor (t) and the new tolerance factor (τ), a system can crystallize in a perovskite structure (corner sharing) if $0.71 < t < 1.0$ or $\tau < 4.31$[43,44]. Notably, the structural tolerance factors of the alloys are always bounded by those of the parent halide perovskites. Thus, if the geometric parameters for parent compounds indicates that they can crystallize as perovskite (i.e., corner sharing), the geometric parameters also will indicate that the resulting alloy crystalize as perovskite, a condition observed in halogen-mixed alloys.

We also calculated the stability with respect to the parent's compounds of the alloys using the mixing enthalpy, defined by Eq. [2]. E_{Tot}^{α} is the total energy of alloy parent α, that is represented here by $CsPbI_3$; E_{Tot}^{β} is the total energy of alloy parent β that is represented here by $CsPbBr_3$; and E_{Tot}^{γ} is the total energy of alloy parent γ that is represented here by CsPbCl3. The parent compounds are taken at their own free-space unit cell equilibrium volume (lattice constant shown in Table I). The indices x and y are the alloy concentration of $CsPb(I_xBr_yCl_{1-x-y})_3$. The results of mixing enthalpy of $CsPb(I_xBr_yCl_{1-x-y})_3$ are shown in Fig. 2(c).

The alloy mixing enthalpy strongly depends on the atomic radius of the halogens. When the alloy is composed of elements with similar atomic radii, such as I and Br, the mixing enthalpy remains below 50 meV/f.u., suggesting that the system can form. This trend is well-documented both experimentally and theoretically in the literature, with numerous reports on the successful synthesis of I-Br mixed alloys[7,10]. A similar behavior is observed for Br and Cl mixing, as shown on the triangular diagram in Fig. 2(c). However, when there is a large disparity in halogen radii, as in the I-Cl combination, the mixing enthalpy increases significantly. For example, Fig. 2(c) shows that ΔH exceeds 100 meV/f.u. for I-Cl compositions near 50%-50%. Despite the choice

of corner-sharing structures suggested by the tolerance factors t and τ, the calculated mixing enthalpy indicates that I-Cl alloys are challenging to form except near the triangle corners.

Alloying Br into and I-Cl alloy, creating a triple halogen mixture, reduces the mixing enthalpy of the halide perovskite. This effect arises from a better balance in the average halogen radii, minimizing the structural strain, i.e., more uniform radius variations minimize octahedral distortions and strain, thereby improving stability. These findings align well with recent experimental data, which suggests that the perovskite structure may not be the most stable phase in the red region of Fig. 2(c)[11].

Thus, for halogen-mixed alloys, the band gap can be estimated from the parent compounds using a linear interpolation based on the alloy composition. Additionally, alloy formation is more favorable when the difference in halogen atomic radii is minimal; a more homogeneous halogen radius distribution reduces the octahedral rotation difference across all the sites, and the mixing enthalpy tends to be small by minimizing internal strain, thereby increasing the chance of successful alloy synthesis.

B. Alloying multiple Alkali cations on the A-Sublattice $(Cs_xRb_yK_{1-x-y})PbBr_3$

Absolute magnitude of the band gaps of alkali perovskite A-site random alloys. The second main category of halide perovskite alloy formation is alkaline mixing, where alkaline metals occupy the A-site of the perovskite structure. Positioned at the center of the cubicoctahedral environment, these monovalent donors contribute to enhanced stability by reducing perovskite strain—an effect particularly beneficial when the A-site contains organic molecules like methylammonium or formamidinium. In this section, however, we focus exclusively on inorganic alkaline-mixed alloys, specifically those based on $(Cs_xRb_yK_{1-x-y})PbBr_3$ to explore the general trends.

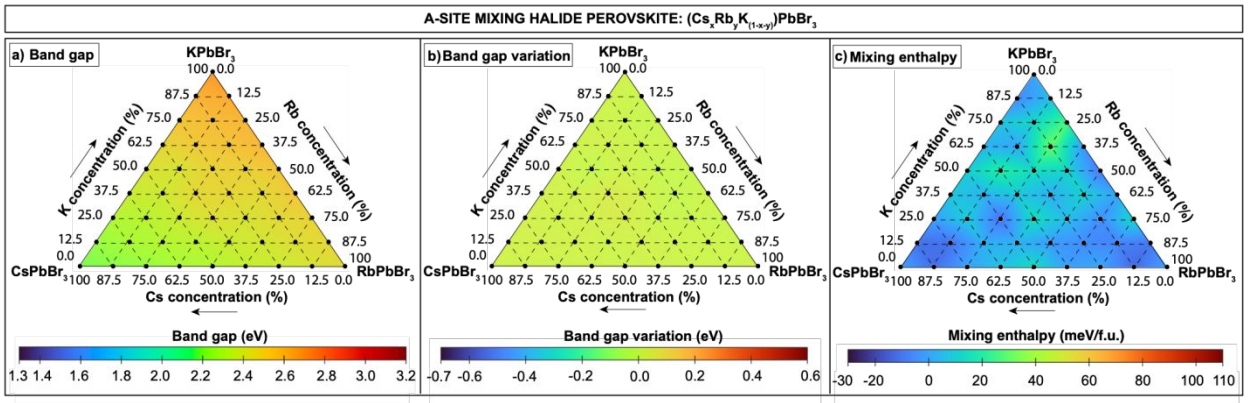

Figure 3: A-site halogen mixing alloys, using as example $(Cs_xRb_yK_{1-x-y})PbBr_3$. (a) Absolute magnitude of Band gaps for alkaline perovskite alloys (b) Band gap variation according to Eq. 1. (c) Alloy mixing enthalpy calculated using Eq. 2.

In halide perovskites, most alkaline atoms occupying the A-site in ABX_3 do not significantly contribute to the states near the band edges, for both valence and conduction band, as illustrated in Fig. 1. The occupied states of A-site atoms are typically located deep within the valence band, while their unoccupied states appear high in the conduction band[24]. An exception occurs with non-alkaline A-site atoms that have ns^2 lone pairs in their valence, such as In or Tl[24], which is not the case in this study. Consequently, the states of Cs, Rb, and K are positioned far from the band edges.

If we consider only the energy levels of alkaline states in the A-site, they should not alter the band gap across different alkaline-mixed alloys composition. However, Fig. 3(a) shows that the band gap of $(Cs_xRb_yK_{1-x-y})CsBr_3$ changes by approximately 0.4 eV, varying from the smallest gap in $CsPbBr_3$ (2.23 eV) to the largest in $KPbBr_3$ (2.66 eV). This band gap variation across the

alloy composition is primarily due to two factors: (i) strain within the octahedra, which increases octahedral rotations and thereby reduces coupling between Pb and Br orbitals[45]; and (ii) changes in cell volume arising from differences in alkaline ionic radii. As with halogen-mixed alloys, the band gap in alkaline-mixed alloys changes gradually smooth rather than abruptly, with no valleys or peaks observed in the band gap distribution in Fig. 3(a).

Deviation of the band gaps of halide perovskite A-site random alloys from the composition weighted averages. We also examined the band gap variation relative to the linear interpolation of the parent alloys (following the Eq. [1]), shown in Fig. 3(b). The maximum band gap variation is in the limit of -40 meV to 40 meV, which represent less than (±)5% of the liner interpolated parents band gap. Therefore, the band gap for alkaline-mixed alloys can also be reliably estimated from a linear interpolation of the band gap of parent compounds.

Mixing enthalpies and structural stability of halide perovskite A-site random alloys. In analyzing the structural stability (geometry) of alkaline-mixed alloys, all parent compounds—$CsPbBr_3$, $RbPbBr_3$, and $KPbBr_3$—are predicted to crystalize in the corner-sharing perovskite structures according to the geometrical Goldschmidt tolerance factor t, as t falls between 0.71 and 1. However, the new tolerance factor τ suggests that $RbPbBr_3$ and $KPbBr_3$ may be unstable in the perovskite structure, as $\tau > 4.31$[44]. Experimentally, only $CsPbBr_3$ has been reported in the perovskite structure, that is considered stable in perovskite according to both t and τ.

To deeply investigate the alkaline-mixed alloy stability, we compute the mixing enthalpy using the Eq. [2], substituting E_{Tot}^{α} as the total energy of alloy $CsPbBr_3$; E_{Tot}^{β} the total energy of alloy $RbPbBr_3$ and E_{Tot}^{γ} the total energy of alloy $KPbBr_3$. Note that all the reference alloys parents are calculated in the cubic polymorphous cell. The mixing enthalpy for $(Cs_xRb_yK_{1-x-y})CsBr_3$ is shown in Fig. 3(c).

Compared to halogen-mixed alloys, the mixing enthalpy for alkaline-mixed alloys is relatively low, with a maximum ΔH of approximately 30 meV/f.u. in $(Cs_xRb_yK_{1-x-y})CsBr_3$, which is three times lower than the highest ΔH observed in halogen mixing as in $CsPb(I_xBr_yCl_{1-x-y})_3$. Additionally, the phase diagram for mixing enthalpy in alkaline-mixed alloys reveals regions where $\Delta H < 0$, potentially indicating long-range ordered configurations with high symmetry in the local arrangement of A-site atoms. We will discuss the case of ordered perovskite in Section (3.5), focusing on double perovskite that is composed by 50%-50% concentration.

Combining the results for mixing enthalpy with the geometric stability criteria from the Goldschmidt tolerance factor t and the new factor τ, alkaline-mixed alloys based on $(Cs_xRb_yK_{1-x-y})CsBr_3$ could likely be synthesized, especially near the $CsPbBr_3$ corner of the triangle in Fig. 3(c). In fact, some experimental results can introduce small concentration of Rb in $CsPbBr_3$ halide perovskites[46]. However, it is important to note that the mixing enthalpy was calculated with respect to the cubic halide perovskite phase. If the real ground states of $RbPbBr_3$ and $KPbBr_3$ have much lower formation energies than the perovskite structure, this information could impact the calculated mixing enthalpy.

Therefore, we can summarize two key points for alkaline alloy mixing: (i) Alkali ionic radii and volume play crucial roles in the band gap variation of $(Cs_xRb_yK_{1-x-y})CsBr_3$, primarily by indirectly influencing octahedral rotations, with the band gap changing smoothly with alkaline concentration. (ii) Mixing enthalpy for alkali alloys is low when compared to halogen mixing alloys, suggesting that a broad range of alkaline compositions could be synthesized.

C. Alloying Multiple Column IV atoms on the B-Sublattice: $Cs(Pb_xSn_yGe_{1-x-y})Br_3$

Absolute Band gaps of random Column IV perovskite alloys on the B sublattice. Atoms of Column-IV group occupy the B-site in ABX_3 halide perovskites, positioned at the center of an octahedron coordinated with six halogen atoms. The most common elements on this site are Pb or Sn, both relatively heavy and typically found in oxidation states of 4+ and 2+. In the 2+ state, as seen in halide perovskites, a ns^2 lone pair forms and hybridizes with halogen p-orbitals, contributing states near the VBM[24]. The conduction band, nevertheless, is created by the unoccupied p-orbitals of the B-site atom. Consequently, the B-site element plays a critical role in defining the band edge states, as illustrated in Fig. 1, and directly influences the band gap of halide perovskites. In this study, we explore alloys formed by combining Pb, Sn, and Ge, elements from group IV, at the B site, creating the alloy $Cs(Pb_xSn_yGe_{1-x-y})Br_3$.

Fig. 4(a) presents the band gap distribution in the triangle phase diagram for triple-mixed B-site atoms. As shown in Table I, $CsGeBr_3$ and $CsSnBr_3$ have similar band gaps, resulting in alloy $Cs(Ge_xSn_{1-x})Br_3$ with the minimal band gap variation across different *x* composition. The most substantial band gap variation occurs along the left edge in the triangle phase diagram, that represent the mixing between of $CsPbBr_3$ and $CsGeBr_3$. Across the full phase diagram, the alloy band gaps are confined by the minimum value of $CsGeBr_3$ (1.37 eV) and the maximum of $CsPbBr_3$ (2.23 eV). However, unlike previously discussed alloys (halogen and alkaline mixing), the B-site mixed alloys exhibit a distinct behavior when compared to the linear interpolation of the parent alloy band gaps.

Deviation of the band gaps of halide perovskite B-site random alloys from the composition weighted averages. In Fig. 4(b), it is illustrated the variation in band gap compared to the linear interpolation of the parent alloy band gaps, following the Eq. 1. Notably, along the base of the triangle representing the alloy $Cs(Pb_xSn_{1-x})Br_3$, there is a downward bowing in the band gap. This is observed by the negative band gap variation (light blue color ~250 meV). For $Cs(Pb_xSn_{1-x})Br_3$ compositions with x = 0.25, the corresponding band gap of 1.51 eV is actually smaller than that of both parent compounds—$CsPbBr_3$ (2.23 eV) and $CsSnBr_3$ (1.53 eV). This observation aligns with previous studies and is attributed to the band alignment of the parent materials[9,12]. As noted, the VBM and CBM of $CsPbBr_3$ and $CsSnBr_3$ derive from the B-site *s*-orbitals and *p*-orbitals, respectively, as illustrated in Fig. 1. On an absolute energy scale, the valence band of $CsSnBr_3$ is higher than that of $CsPbBr_3$, while $CsPbBr_3$ has a lower conduction band edge compared to $CsSnBr_3$. Alloying results in band edges influenced by different B-site contributions, the valence band primarily reflects Sn *s*-orbitals, and the conduction band is dominated by Pb *p*-orbitals. This configuration leads to a downward bowing of the band gap, achieving values smaller than the parent compounds for low Pb concentrations in $Cs(Pb_xSn_{1-x})Br_3$.

The incorporation of Ge in the group-IV alloys leads to an upward bowing of the band gap. This behavior is likely due to a different band alignment among the parent compounds. In $Cs(Pb_xGe_{1-x})Br_3$, the valence band is primarily composed of Ge *s*-orbitals, while the conduction band arises from a hybridization of Ge *p*-orbitals and Pb *p*-orbitals. This alignment suggests that the conduction bands of $CsPbBr_3$ and $CsGeBr_3$ are at similar energy levels, while the valence band of $CsGeBr_3$ is positioned higher than that of $CsPbBr_3$. Consequently, adding Ge to the system prevents downward bowing, resulting in a band gap that aligns more closely with the linear interpolation of the parent compounds. This is well observed by the green/yellow color in Fig. 4(b), indicating a positive band gap variation with respect to the linear parents' band gap interpolation.

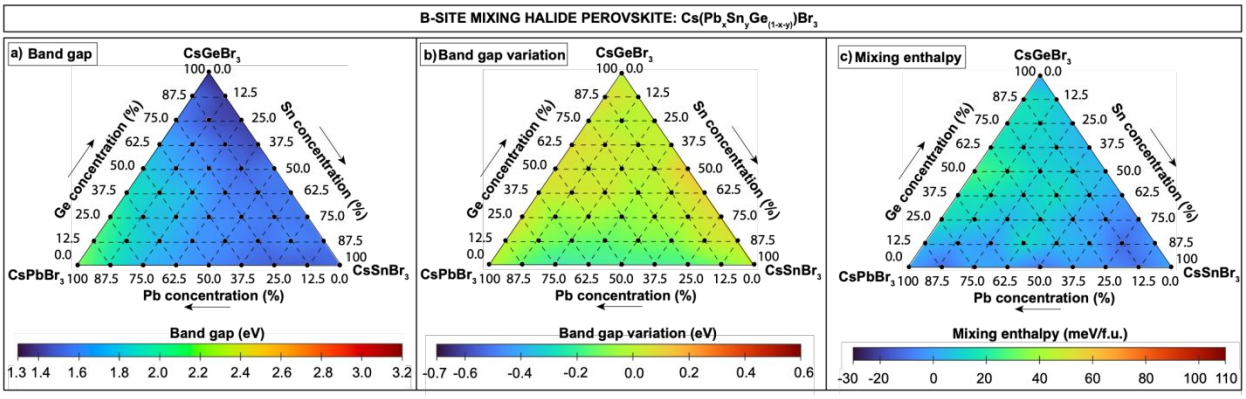

Figure 4: B-site group IV mixing alloys, using as example $Cs(Pb_xSn_yGe_{1-x-y})Br_3$. (a) Absolute magnitude of Band gaps for group IV perovskite alloys (b) Band gap variation according to Eq. 1. (c) Alloy mixing enthalpy calculate using Eq. 2.

Mixing enthalpies and structural stability of halide perovskite B-site random alloys. Table I shows the corner-sharing geometric stability of various group-IV parent alloys, as indicated by the Goldschmidt tolerance factor t and the new tolerance factor τ. According to the t values, $CsSnBr_3$ and $CsGeBr_3$ may not be stable in the perovskite structure, which contrasts with the τ values, both of which are below the stability threshold of 4.31. In reality, $CsSnBr_3$ is a perovskite structure that has been experimentally confirmed, and some experimental evidence suggests that $CsGeBr_3$ may also form under suitable conditions[47].

To improve the halide perovskite alloy stability discussion, we also compute the mixing enthalpy for group-IV substitution on the B sublattice using Eq. [2]. E^{α}_{Tot} is the total energy of alloy $CsPbBr_3$; E^{β}_{Tot} the total energy of alloy $CsSnBr_3$ and E^{γ}_{Tot} the total energy of alloy $CsGeBr_3$, and the results are shown in Fig. 4(c). Recall that the parent reference compounds are calculated in the polymorphous cubic perovskites. Consistent with previous findings, the left edge of the triangular phase diagram of Fig. 4(c) indicates the path with the largest variation in B-site atomic radii. This region shows the highest mixing enthalpy, with maximum ΔH around 30 meV/f.u., a value that is comparable to what is calculated in alkaline-mixed alloys and three times lower than the maximum mixing enthalpy for halogen-mixed alloys. Near $CsSnBr_3$ [right corner of Fig. 4(c)], a region with low concentrations of Pb and Ge, and composition $Cs(Pb_{0.125}Sn_{0.75}Ge_{0.125})Br_3$ forms a "valley" in the mixing enthalpy phase diagram, which may suggest potential candidate for long-range ordering. In Section (3.5), we also analyze the possibility to form collum-IV long-range ordered double perovskites.

Therefore, mixing different group-IV elements at the B site of halide perovskites results in band gap variations that differ significantly from halogen or alkaline mixing. For instance, in $Cs(Pb_xSn_{1-x})Br_3$, a downward bowing of the band gap occurs. This downward bowing offers a promising approach to reduce the band gap and enhance optical absorption, similar to the effect seen in $CdTe_xSe_{1-x}$ alloys[13]. Additionally, it provides a pathway to lower Pb concentration in halide perovskites. Mixing enthalpy calculations suggest that alloys like $Cs(Pb_xSn_yGe_{1-x-y})Br_3$ are feasible to form; however, alloys with significant atomic radius differences among B-site atoms, such as those with intermediate Pb and Ge concentrations, may not be stable. This is a consequence for the large disparity between local chemical environments.

D Hetero-valent Halide Perovskite alloys on the B sublattice: $Cs(Pb_xSn_yCd_{1-x-y})Br_3$

The mixing of hetero-valent elements on one site of halide perovskites can modify the physics trend of the electronic structure and create new properties, such as band gap variation, mixing enthalpy stability, etc. All of them are accessed just by composition control. In our case, we consider two well-known parent compounds, $CsPbBr_3$ and $CsSnBr_3$, and introduce a third

parent compound $CsCdBr_3$, forming the alloy $Cs(Pb_xSn_yCd_{1-x-y})Br_3$. Here Cd has occupied *s*-orbitals but no *p*-orbitals, unlike Ge and Sn, and this orbital contribution changes drastically the band edge orbital composition shown in Fig. 1.

It is important to note that the reference polymorphous cubic perovskite $CsCdBr_3$ do not represent the experimentally most stable phase, and the ground state for $CsGeBr_3$ is the hexagonal P63/mmc structure. However, the Goldschmidt tolerance factor t and the new tolerance factor τ for $CsCdBr_3$ suggest that it can crystallize in the perovskite structure. Previous calculations reported in Materials Project[48] indicate that $CsCdBr_3$ in the perovskite configuration exhibits a very low formation energy, comparable to that of the ground state of the non-perovskite hexagonal structure. Furthermore, Cd can be successfully incorporated into halide perovskite alloys while preserving stable perovskite configurations, as demonstrated by experimental studies[49,50]. These investigations suggest that up to 25% Cd can be integrated into a nanoscale $CsPbBr_3$ perovskite. Thus, $Cs(Pb_xSn_yCd_{1-x-y})Br_3$ can in principle form for some compositions.

Absolute band gaps of random hetero-valent halide perovskite B-site alloys. Before discussing the results for the alloys band gap, it is important to highlight a few key aspects of the electronic structure of the parent compounds that define the corners of the triangle in Fig. 5(a). As shown in Table I, the band gap of $CsCdBr_3$, approximately 2.99 eV, is significantly higher than that of $CsPbBr_3$ (2.23 eV) and $CsSnBr_3$ (1.53 eV). Furthermore, the band edges orbital character (BEOC) of $CsCdBr_3$ are composed of different orbitals: The valence band primarily consists of Br *p*-orbitals, lacking the ns^2 lone pairs found in Pb and Sn, while the conduction band is primarily composed of Cd *s*-orbitals. This suggests that spin-orbit coupling (SOC) will have a minimal impact on $CsCdBr_3$, in contrast to the other two parents compounds: $CsPbBr_3$ and $CsSnBr_3$[24]. The nature of the band gap is also different, while the systems $CsPbBr_3$ and $CsSnBr_3$ have a direct band gap with VBM and CBM at R point, the $CsCdBr_3$ have an indirect band gap with VBM at R point and CBM at Γ point.

In Fig. 5(a), we present the band gap of $Cs(Pb_xSn_yCd_{1-x-y})Br_3$ alloy in the compositional triangle. The base of the triangle reflects the results discussed in the previous section concerning group-IV alloys, as it describes the binary alloy $Cs(Pb_xSn_{1-x})Br_3$. The incorporation of Cd into the halide perovskite, forming alloys, expands the band gap, creating a region with a significantly wider band gap near the 50%-50% concentration of Pb and Cd, as indicated by the red area in Fig. 5(a). In this region, the band gap of $Cs(Pb_{0.5}Cd_{0.5})Br_3$ reaches 3.21 eV. Therefore, in this particular case, the alloy band gap exceeds that of the parent compounds, i.e., the alloy band gap is not confined between the smallest parent band gap ($CsSnBr_3$ being 1.53 eV) and the largest parent band gap ($CsCdBr_3$ being 2.99 eV).

Deviation of the band gaps of hetero-valent halide perovskite B-site random alloys from the composition. The fluctuation of the band gap is also evident in Fig. 5(b), which illustrates the difference between the calculated alloy band gap and the linear interpolation of the parent compounds, as defined by Eq. 1. It is apparent that, across the compositions of Cd and Pb, there is a significant variation in the band gap, with an upward deviation from the linear interpolation that can reach up to 0.6 eV for $Cs(Pb_{0.5}Cd_{0.5})Br_3$. Such a substantial upward variation is uncommon in alloy materials and contrasts sharply with the downward band gap deviations that have been widely reported in numerous cases.

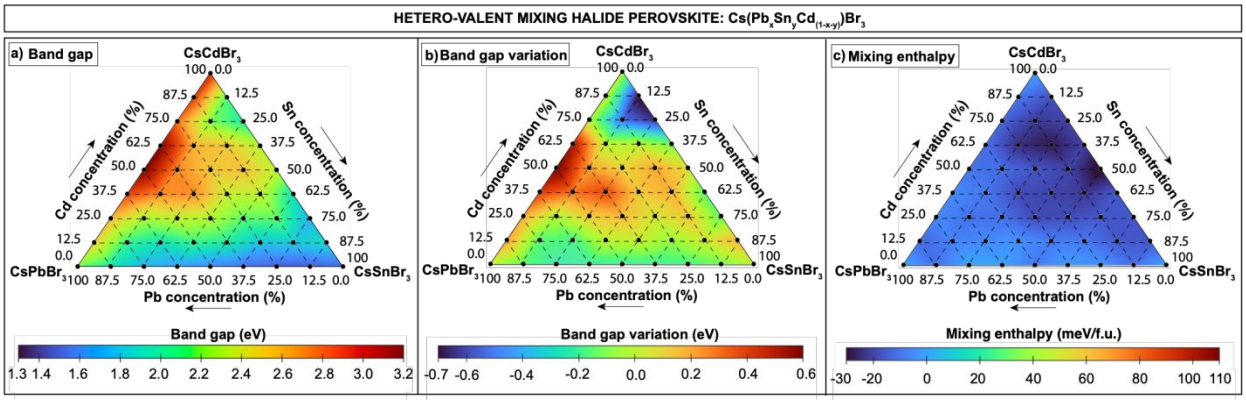

Figure 5: B-site hetero-valent mixing alloys, using as example $Cs(Pb_xSn_yCd_{1-x-y})Br_3$. (a) Absolute magnitude of Band gaps for group IV perovskite alloys (b) Band gap variation according to Eq. 1. (c) Alloy mixing enthalpy calculated using Eq. 2.

To further investigate the variation in the band gap, we focus our analysis on the Pb-Cd alloy composition, $Cs(Pb_xCd_{1-x})Br_3$, for clearer interpretation. In Fig. 6, we present the calculated band gap values both with and without considering spin-orbit coupling (SOC).

The variation of the band gap with the addition of SOC represents the values plotted along the left edge of Fig. 5(a). As previously noted, systems based on Pb exhibit significant SOC, making its inclusion in DFT calculations essential for accurately capturing the physics and correct band gap of compounds like $CsPbBr_3$. In contrast, SOC has a minimal impact in $CsCdBr_3$, as the Br *p*-orbitals in the valence band and the Cd *s*-orbitals in the conduction band are not significantly influenced by this effect. When forming an Pb-Cd alloy, the mixing of orbitals in both the valence and conduction bands occurs. The calculated band gap values with and without SOC indicate that for compositions with $x < 0.375$ in $Cs(Cd_xPb_{1-x})Br_3$ (blue area of Fig. 6), the band edges are primarily characterized by Pb orbitals, while for $x > 0.375$ (red area Fig. 6), Cd orbitals dominate (the two lines are nearly coincident). This demonstrates a transition in the orbital character at the band gap edges based on the alloy's chemical composition. As the influence of Cd increases, the volume of the alloy is affected by the concentration of Pb, which directly influences the overlap between the Cd and Br states, resulting in an increase in the band gap. In addition, the Cd concentration also affect the nature of the band gap, in the blue region there is a tendency for direct band gap, while the red region the indirect band gap. At specific concentrations and volumes, the band gap of the alloy can surpass those of both parent compounds, resulting in a large upward bowing.

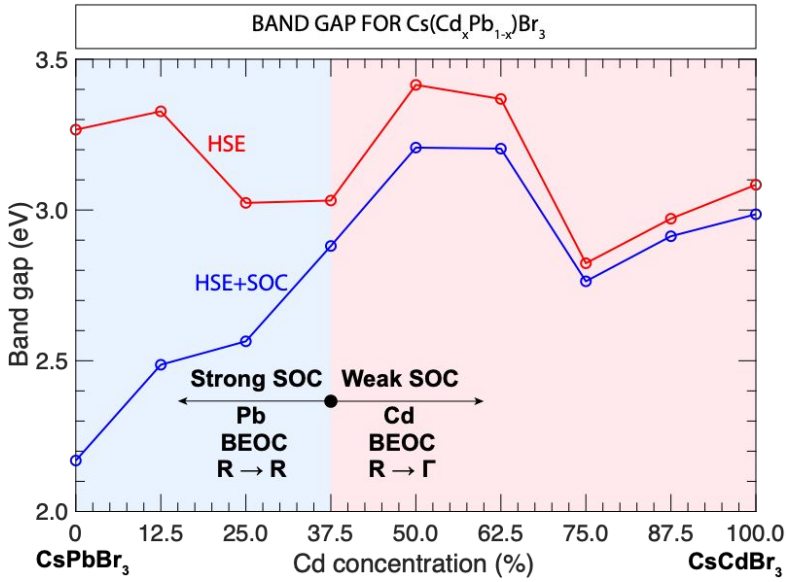

Figure 6: Band gap for $Cs(Cd_xPb_{1-x})Br_3$ varying Cd concentrations (x), calculated using HSE (red) and HSE+SOC (blue) functionals. The blue region indicates concentrations where Pb dominates the band edge orbital character (BEOC), with a strong SOC effect, and direct band gap R to R point, while the red region represents concentrations where Cd contributes to the BEOC, resulting in a weak SOC and indirect band gap R to Γ point.

Mixing enthalpies and structural stability of random hetero-valent halide perovskite alloys on the B. We also investigate the stability of the $Cs(Pb_xSn_yCd_{1-x-y})Br_3$ alloy; however, this discussion will focus on the dilution of $CsCdBr_3$, into $CsPbBr_3$ and $CsSnBr_3$, since the alloy $Cs(Pb_xSn_{1-x})Br_3$ were addressed in the previous section. In Fig. 5(d), we present the mixing enthalpy for $Cs(Pb_xSn_yCd_{1-x-y})Br_3$ across various B-site compositions. For this alloy, most systems exhibit $\Delta H < 0$, indicating two possible conditions: (i) the reference structure of cubic polymorphous perovskite $CsCdBr_3$ may not adequately describe the system, or (ii) there is a tendency to form long-range ordered structures, i.e., high-symmetry configurations. Notably, in the case of condition (ii), we highlight a significant valley in the mixing enthalpy for $Cs(Sn_{0.5}Cd_{0.5})Br_3$, representing a 50%-50% composition of Sn and Cd. This configuration can be associated with double perovskites, which feature a highly symmetrical B-site organization, similar to Cs_2BiAgI_6. This double perovskite configuration will be addressed in the next section.

Therefore, our analysis of hetero-valent halide perovskite alloys reveals intriguing physical phenomena in the band gap of $Cs(Pb_xSn_yCd_{1-x-y})Br_3$. At intermediate concentrations of Pb and Cd, we observe a significant upward bowing of the band gap, an effect that is uncommon in semiconductor alloys. This behavior arises from a combination of volume expansion (caused by the alloy composition) and changes in the orbital character at the band edges. Moreover, $Cs(Pb_xSn_yCd_{1-x-y})Br_3$ may exhibit long-range ordered compositions, particularly in the alloy composition with a 50%-50% ratio of Sn and Cd.

E Random Alloys vs. ordered double perovskites

In the previous sections, we examined the stability of alloys across different sites and concentrations, referencing the polymorphous cubic perovskite phase at finite temperature. Here, we explore the competition between alloys of perovskite (non-ordered) and ordered perovskite structures. Specifically, we compare the energetic stability of 50%-50% binary perovskite alloys with their corresponding ordered double perovskites. To ensure consistency, we use the same lattice constant for both the alloy and ordered structures while incorporating polymorphous cubic-envelope symmetry breaking. The supercells are designed to capture polymorphous features, comprising 160 atoms for alloys and 40 atoms for ordered structures.

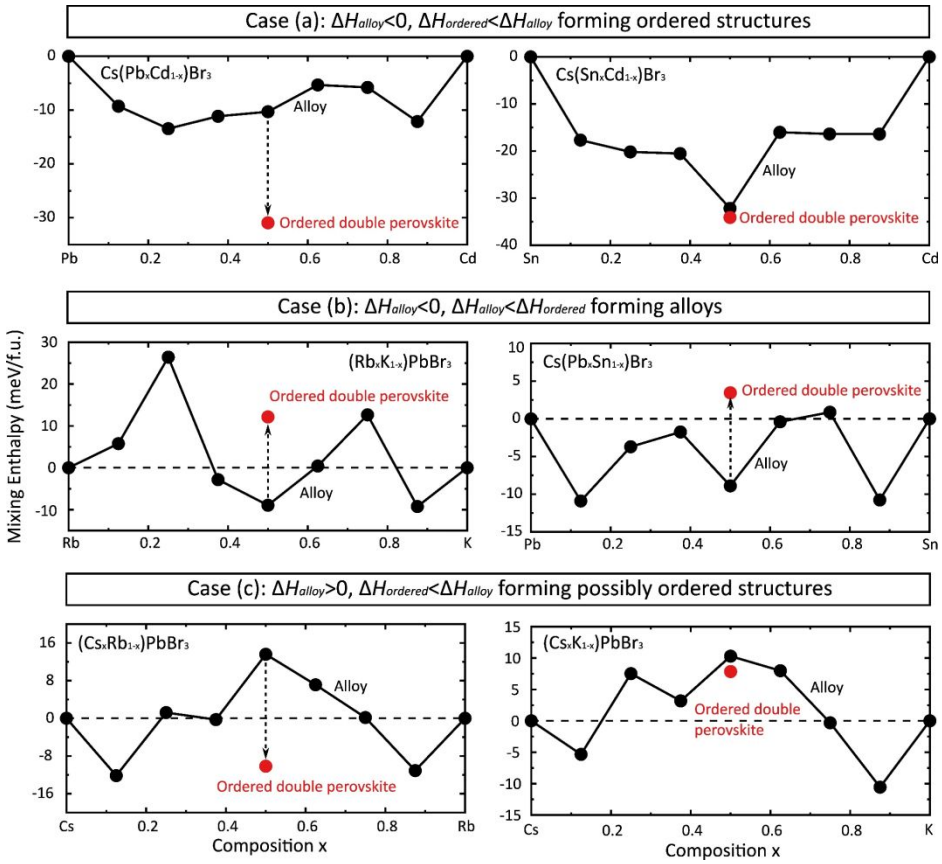

Figure 7: Mixing enthalpies at different compositions x for Case (a) $\Delta H_{alloy} < 0$ and $\Delta H_{ordered} < \Delta H_{alloy}$ forming ordered double perovskites, Case (b) $\Delta H_{alloy} < 0$ and $\Delta H_{alloy} < \Delta H_{ordered}$ forming alloys, and Case (c) $\Delta H_{alloy} > 0$ and $\Delta H_{ordered} < \Delta H_{alloy}$ forming possibly ordered double perovskites.

The competition between alloys and ordered structures is governed by two key principles: (i) whether the perovskite alloys have a negative mixing enthalpy ($\Delta H_{alloy} < 0$), indicating their stability relative to single perovskites; (ii) whether the ordered double perovskites have a lower mixing enthalpy than the alloys ($\Delta H_{ordered} < \Delta H_{alloy}$), suggesting the potential formation of ordered structures from the alloys. These two principles define four possible scenarios, which we summarize Fig. 8 and discussed in the sequence. The corresponding mixing enthalpies are presented in Fig. 7.

Case (a) $\Delta H_{alloy} < 0 \mid \Delta H_{ordered} < \Delta H_{alloy}$	Case (c) $\Delta H_{alloy} > 0 \mid \Delta H_{ordered} < \Delta H_{alloy}$
$Cs(Pb_{0.5}Cd_{0.5})Br_3$ $Cs(Sn_{0.5}Cd_{0.5})Br_3$	$(Cs_{0.5}Rb_{0.5})PbBr_3$ $(Cs_{0.5}K_{0.5})PbBr_3$
Case (b) $\Delta H_{alloy} < 0 \mid \Delta H_{ordered} > \Delta H_{alloy}$	**Case (d)** $\Delta H_{alloy} > 0 \mid \Delta H_{ordered} > \Delta H_{alloy}$
$(Cs_{0.5}K_{0.5})PbBr_3$ $Cs(Pb_{0.5}Sn_{0.5})Br_3$	$CsPb(I_{0.5}Br_{0.5})_3$ $CsPb(I_{0.5}Cl_{0.5})_3$ $CsPb(Br_{0.5}Cl_{0.5})_3$ $Cs(Pb_{0.5}Ge_{0.5})Br_3$ $Cs(Sn_{0.5}Ge_{0.5})Br_3$

Figure 8: Classification of perovskite alloys and ordered double perovskites based on (i) whether perovskite alloys have a negative mixing enthalpy ($\Delta H_{alloy} < 0$) and (ii) whether ordered double perovskites have a lower mixing enthalpy than alloys ($\Delta H_{ordered} < \Delta H_{alloy}$).

Case (a): $\Delta H_{alloy} < 0$ and $\Delta H_{ordered} < \Delta H_{alloy}$. The perovskite alloys are stable relative to the single perovskites, however, the ordered double perovskites exhibit even lower energies than the alloys. Systems belonging to this case tend to form ordered double perovskites. Examples are $Cs(Pb_{0.5}Cd_{0.5})Br_3$ and $Cs(Sn_{0.5}Cd_{0.5})Br_3$ both of which involve B-site mixing with hetero-valent elements. The charge transfer between the Group-IV element (Pb and Sn) and Cd plays an important role in the formation of ordered double perovskite structures. Fig. 7(a) shows that the ordered $Cs_2(PbCd)Br_6$ has a mixing enthalpy of 21 meV/f.u. lower than the alloy $Cs(Pb_{0.5}Cd_{0.5})Br_3$, and the ordered $Cs_2(SnCd)Br_6$ has a mixing enthalpy of 2 meV/f.u. lower than the alloy $Cs(Sn_{0.5}Cd_{0.5})Br_3$.

Case (b): $\Delta H_{alloy} < 0$ and $\Delta H_{alloy} < \Delta H_{ordered}$. The perovskite alloys are stable relative to the single perovskites, and also have lower energies than the ordered double perovskites. Systems belonging to this case tend to form alloys instead of ordered structures. Examples are $(Rb_{0.5}K_{0.5})PbBr_3$ and $Cs(Pb_{0.5}Sn_{0.5})Br_3$, which have A-site and B-site mixing with isovalent elements, respectively. Fig. 7(b) shows that the alloy $(Rb_{0.5}K_{0.5})PbBr_3$ has a mixing enthalpy of 21 meV/f.u. lower than the ordered $(RbK)Pb_2Br_6$, and the alloy $Cs(Pb_{0.5}Sn_{0.5})Br_3$ has a mixing enthalpy of 12 meV/f.u. lower than the ordered $Cs_2(PbSn)Br_6$.

Case (c): $\Delta H_{alloy} > 0$ and $\Delta H_{ordered} < \Delta H_{alloy}$. The perovskite alloys are not stable relative to the single perovskites, but the ordered double perovskites can either be stable or unstable relative to the single perovskites. Disregarding the configurational entropy, systems belonging to this case cannot form alloys, but still have a chance to form ordered double perovskites, such as $(Cs_{0.5}Rb_{0.5})PbBr_3$. Another possibility is that the system forms neither alloy nor ordered structure, such as $(Cs_{0.5}K_{0.5})PbBr_3$. Fig. 7© shows that the ordered $(CsRb)Pb_2Br_6$ has a negative mixing enthalpy of -10 meV/f.u. which is 24 meV/f.u. lower than the mixing enthalpy of the alloy $(Cs_{0.5}Rb_{0.5})PbBr_3$, but the ordered $(CsK)Pb_2Br_6$ has a positive mixing enthalpy of 8 meV/f.u. which is 2 meV/f.u. lower than the mixing enthalpy of the alloy $(Cs_{0.5}K_{0.5})PbBr_3$.

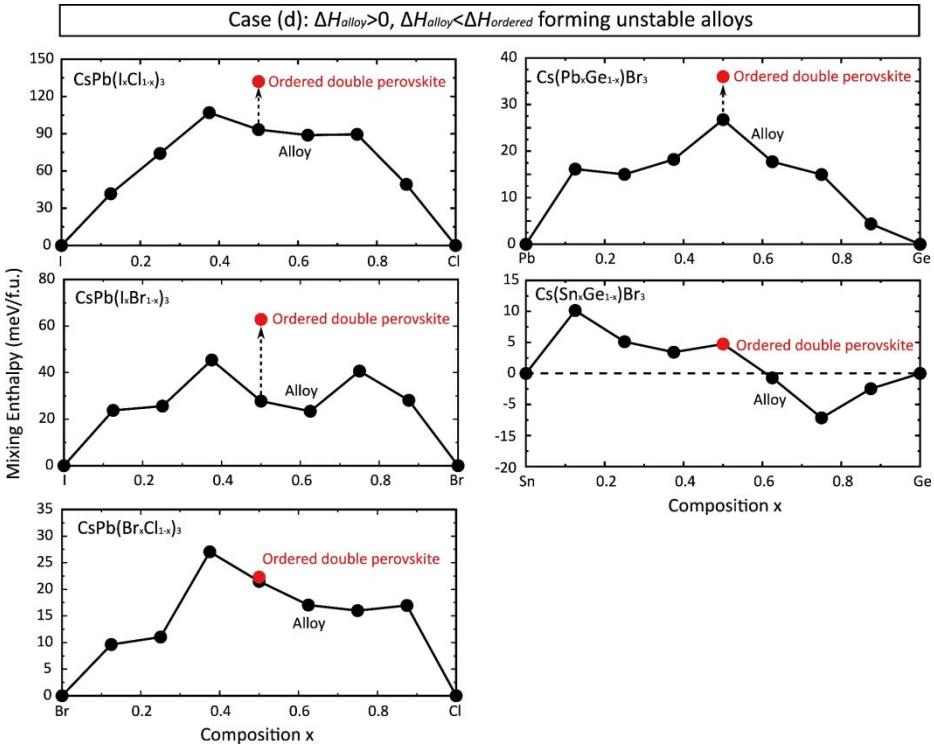

Figure 9: Mixing enthalpies at different composition x for Case (d) $\Delta H_{alloy} > 0$ and $\Delta H_{alloy} < \Delta H_{ordered}$ forming unstable alloys.

Case (d): $\Delta H_{alloy} > 0$ and $\Delta H_{alloy} < \Delta H_{ordered}$. The perovskite alloys are not stable relative to the single perovskites, while the ordered double perovskites are even more unstable. Systems belonging to this case only forms unstable alloys. Examples are $CsPb(I_{0.5}Br_{0.5})_3$, $CsPb(I_{0.5}Cl_{0.5})_3$, $CsPb(Br_{0.5}Cl_{0.5})_3$, $Cs(Pb_{0.5}Ge_{0.5})Br_3$, and $Cs(Sn_{0.5}Ge_{0.5})Br_3$. It appears that all the X-site mixing systems and most isovalent B-site mixing systems belong to this trivial case. Fig. 9 shows that the magnitudes of mixing enthalpy of these ordered double perovskites are tens to over one hundred meV/f.u. larger than the alloy configuration.

Therefore, we computed the ordered double perovskite systems to compare their relative stability with the alloy configuration. It is important to note that our analysis is based merely on mixing enthalpy, without considering entropy contributions (configurational, vibrational, and others). Entropy likely plays a significant role in stabilizing the alloy configuration relative to both single perovskites and ordered double perovskites. A notable example is X-site mixing, where nearly all 50%-50% halogen compositions (Cl, Br, and I) can be synthesized, despite our theoretical results indicating a positive mixing enthalpy.

IV. Conclusions

In summary, we investigated triple-mixed halide perovskites with various chemical compositions and in different site substitutions and we analyze the effects of different chemical composition in the electronic structure and the stability. For halogen mixing, atomic radii differences play a crucial role in both band gap and mixing enthalpy. Intermediate mixing of Cl and I introduces significant strain, increasing instability in the halide perovskite (HP) structure. Alkaline atoms at the A site do not alter the band edge orbital characters but affect unit cell volume, influencing both band gap and mixing enthalpy. In these two cases, halogen and alkaline mixed, the band gap can be fine-tuned by the HP composition, and the band gap can be estimated by a linear interpolation of the parents' compounds. For group IV mixing at the B site (Ge, Sn and Pb), the chemical composition

significantly impacts the band edges orbital characters (BEOC), thus affecting band gap and mixing enthalpy. In Pb-Sn mixed alloys, a downward band gap bowing is observed, while the addition of Ge reduces this effect. Introducing hetero-valent atoms, such as Cd, at the B site creates unusual band gap behavior, including a significant upward bowing uncommon in semiconductor alloys. This upward bowing results from BEOC changes from Pb to Cd, where SOC plays a critical role, combined with volume changes due to alloying. In addition, comparing the mixing enthalpy for alloys and double perovskites (ordered system) our results indicate a possible long range ordered double perovskite composed by 50%-50% of Cd-Sn and Cd-Pb. Halide perovskite alloys offer potential use for next-generation solar cells, and this study provides insights into how site-specific mixing influences essential properties like band gap and stability. Nevertheless, it is important to note that point defects—such as vacancies, anti-site, and interstitials atoms—which were not considered in this study, can alter the electronic structure of halide perovskites by introducing deep states within the band gap. This aspect represents an important direction for future investigations.

V. Data availability

Data for this article, including the alloys chemical composition, band gap and total energy, all of them calculated with density functional theory, and are available at Gitbub at https://github.com/fernandopsabino/data_alloys_HP.

VI. Acknowledgement

AZ, FPS, JXX, and XZ: This material is based upon work supported by the U.S. Department of Energy's Office of Energy Efficiency and Renewable Energy (EERE) under the Solar Energy Technologies Office Award Number DE-EE0009615. FPS and GMD also thank FAPESP (grants 2021/14422-0, 2021/11786-1 and 23/09820-2) for financial support, and the National Laboratory for Scientific Computing (LNCC/MCTI, Brazil) for providing HPC resources on the SDumont supercomputer.

VII. References

1 G. E. Eperon, M. T. Hörantner and H. J. Snaith, *Nat Rev Chem*, 2017, **1**, 1–18.
2 N.-G. Park, *Materials Today*, 2015, **18**, 65–72.
3 Y. Rong, Y. Hu, A. Mei, H. Tan, M. I. Saidaminov, S. I. Seok, M. D. McGehee, E. H. Sargent and H. Han, *Science*, 2018, **361**, eaat8235.
4 H. Chen, C. Liu, J. Xu, A. Maxwell, W. Zhou, Y. Yang, Q. Zhou, A. S. R. Bati, H. Wan, Z. Wang, L. Zeng, J. Wang, P. Serles, Y. Liu, S. Teale, Y. Liu, M. I. Saidaminov, M. Li, N. Rolston, S. Hoogland, T. Filleter, M. G. Kanatzidis, B. Chen, Z. Ning and E. H. Sargent, *Science*, 2024, **384**, 189–193.
5 A. K. Jena, A. Kulkarni and T. Miyasaka, *Chem. Rev.*, 2019, **119**, 3036–3103.
6 J. Y. Kim, J.-W. Lee, H. S. Jung, H. Shin and N.-G. Park, *Chem. Rev.*, 2020, **120**, 7867–7918.
7 F. Lehmann, A. Franz, D. M. Többens, S. Levcenco, T. Unold, A. Taubert and S. Schorr, *RSC Adv.*, 2019, **9**, 11151–11159.
8 F. P. Sabino, G. M. Dalpian and A. Zunger, *Advanced Energy Materials*, 2023, **13**, 2301539.
9 G. M. Dalpian, X.-G. Zhao, L. Kazmerski and A. Zunger, *Chem. Mater.*, 2019, **31**, 2497–2506.
10 E. T. Hoke, D. J. Slotcavage, E. R. Dohner, A. R. Bowring, H. I. Karunadasa and M. D. McGehee, *Chem. Sci.*, 2014, **6**, 613–617.
11 J. Jung, Y. Yun, S. W. Yang, H. G. Oh, A.-Y. Jeon, Y. Nam, Y.-W. Heo, W.-S. Chae and S. Lee, *Acta Materialia*, 2023, **246**, 118661.
12 A. Goyal, S. McKechnie, D. Pashov, W. Tumas, M. van Schilfgaarde and V. Stevanović, *Chem. Mater.*, 2018, **30**, 3920–3928.

13 S.-H. Wei and S. B. Zhang, *physica status solidi (b)*, 2002, **229**, 305–310.
14 H. Gao, D. He, Z. Chen, P. Gao, D. He, Z. Li, X. Zhang, J. Xiu, Q. Sun, S. Chen, S.-H. Wei, S.-H. Yu and Z. He, *Science Advances*, 2025, **11**, eads4038.
15 S.-H. Wei and A. Zunger, *Phys. Rev. B*, 1997, **55**, 13605–13610.
16 J. L. Lyons, A. Janotti and C. G. Van de Walle, *Phys. Rev. Lett.*, 2012, **108**, 156403.
17 I. Chatratin, F. P. Sabino, P. Reunchan, S. Limpijumnong, J. B. Varley, C. G. Van de Walle and A. Janotti, *Phys. Rev. Materials*, 2019, **3**, 074604.
18 S. B. Zhang, S.-H. Wei, A. Zunger and H. Katayama-Yoshida, *Phys. Rev. B*, 1998, **57**, 9642–9656.
19 F. P. Sabino, A. Zunger and G. M. Dalpian, *Mater. Horiz.*, 2022, **9**, 791–803.
20 J. Kang and L.-W. Wang, *J. Phys. Chem. Lett.*, 2017, **8**, 489–493.
21 D. Meggiolaro, S. G. Motti, E. Mosconi, A. J. Barker, J. Ball, C. A. R. Perini, F. Deschler, A. Petrozza and F. D. Angelis, *Energy Environ. Sci.*, 2018, **11**, 702–713.
22 X. Zhang, J.-X. Shen, M. E. Turiansky and C. G. V. de Walle, *J. Mater. Chem. A*, 2020, **8**, 12964–12967.
23 X.-G. Zhao, G. M. Dalpian, Z. Wang and A. Zunger, *Phys. Rev. B*, 2020, **101**, 155137.
24 F. P. Sabino, X. G. Zhao, G. M. Dalpian and A. Zunger, *Phys. Rev. B*, 2024, **110**, 035160.
25 X.-G. Zhao, Z. Wang, O. I. Malyi and A. Zunger, *Materials Today*, 2021, **49**, 107–122.
26 J. P. Perdew, K. Burke and M. Ernzerhof, *Phys. Rev. Lett.*, 1996, **77**, 3865–3868.
27 J. Heyd and G. E. Scuseria, *J. Chem. Phys.*, 2004, **120**, 7274–7280.
28 J. Heyd, G. E. Scuseria and M. Ernzerhof, *J. Chem. Phys.*, 2006, **124**, 219906.
29 A. Zunger, S.-H. Wei, L. G. Ferreira and J. E. Bernard, *Phys. Rev. Lett.*, 1990, **65**, 353–356.
30 S.-H. Wei, L. G. Ferreira, J. E. Bernard and A. Zunger, *Phys. Rev. B*, 1990, **42**, 9622–9649.
31 G. Kresse and J. Hafner, *Phys. Rev. B*, 1993, **48**, 13115–13118.
32 G. Kresse and J. Furthmüller, *Phys. Rev. B*, 1996, **54**, 11169–11186.
33 G. Kresse and D. Joubert, *Phys. Rev. B*, 1999, **59**, 1758–1775.
34 P. E. Blöchl, *Phys. Rev. B*, 1994, **50**, 17953–17979.
35 D. M. Trots and S. V. Myagkota, *Journal of Physics and Chemistry of Solids*, 2008, **69**, 2520–2526.
36 L. Protesescu, S. Yakunin, M. I. Bodnarchuk, F. Krieg, R. Caputo, C. H. Hendon, R. X. Yang, A. Walsh and M. V. Kovalenko, *Nano Lett.*, 2015, **15**, 3692–3696.
37 P. Cottingham and R. L. Brutchey, *Chemical Communications*, 2016, **52**, 5246–5249.
38 M. Sebastian, J. A. Peters, C. C. Stoumpos, J. Im, S. S. Kostina, Z. Liu, M. G. Kanatzidis, A. J. Freeman and B. W. Wessels, *Phys. Rev. B*, 2015, **92**, 235210.
39 C. K. Møller, *The structure of perovskite-like cæsium plumbo trihalides*, Munksgaard, København, 1959.
40 Y. He, C. C. Stoumpos, I. Hadar, Z. Luo, K. M. McCall, Z. Liu, D. Y. Chung, B. W. Wessels and M. G. Kanatzidis, *J. Am. Chem. Soc.*, 2021, **143**, 2068–2077.
41 J. D. Donaldson, J. Silver, S. Hadjiminolis and S. D. Ross, *J. Chem. Soc., Dalton Trans.*, 1975, 1500–1506.
42 S. J. Clark, C. D. Flint and J. D. Donaldson, *Journal of Physics and Chemistry of Solids*, 1981, **42**, 133–135.
43 V. M. Goldschmidt, *Naturwissenschaften*, 1926, **14**, 477–485.
44 C. J. Bartel, C. Sutton, B. R. Goldsmith, R. Ouyang, C. B. Musgrave, L. M. Ghiringhelli and M. Scheffler, *Science Advances*, **5**, eaav0693.
45 R. Prasanna, A. Gold-Parker, T. Leijtens, B. Conings, A. Babayigit, H.-G. Boyen, M. F. Toney and M. D. McGehee, *J. Am. Chem. Soc.*, 2017, **139**, 11117–11124.
46 J. Li, X. Du, G. Niu, H. Xie, Y. Chen, Y. Yuan, Y. Gao, H. Xiao, J. Tang, A. Pan and B. Yang, *ACS Appl. Mater. Interfaces*, 2020, **12**, 989–996.
47 D. Yang, G. Zhang, R. Lai, Y. Cheng, Y. Lian, M. Rao, D. Huo, D. Lan, B. Zhao and D. Di, *Nat Commun*, 2021, **12**, 4295.
48 A. Jain, S. P. Ong, G. Hautier, W. Chen, W. D. Richards, S. Dacek, S. Cholia, D. Gunter, D. Skinner, G. Ceder and K. A. Persson, *APL Materials*, 2013, **1**, 011002.
49 M. Imran, J. Ramade, F. Di Stasio, M. De Franco, J. Buha, S. Van Aert, L. Goldoni, S. Lauciello, M. Prato, I. Infante, S. Bals and L. Manna, *Chem. Mater.*, 2020, **32**, 10641–10652.
50 Y. Zhao, C. Shen, L. Ding, J. Liu, W. Xiang and X. Liang, *Optical Materials*, 2020, **107**, 110046.